INTERNATIONAL JOURNAL FOR NUMERICAL METHODS IN FLUIDS
Int. J. Numer. Meth. Fluids 2000; **33**: 175–202

Depth-averaged two-dimensional curvilinear explicit finite analytic model for open-channel flows

Chih-Tsung Hsu*[,1], Keh-Chia Yeh and Jinn-Chuang Yang

Department of Civil Engineering, National Chiao Tung University, 1001 Ta Hsueh Road, Hsinchu, 30050 Taiwan, Republic of China

SUMMARY

A depth-averaged two-dimensional model has been developed in the curvilinear co-ordinate system for free-surface flow problems. The non-linear convective terms of the momentum equations are discretized based on the explicit–finite–analytic method with second-order accuracy in space and first-order accuracy in time. The other terms of the momentum equations, as well as the mass conservation equation, are discretized by the finite difference method. The discretized governing equations are solved in turn, and iteration in each time step is adopted to guarantee the numerical convergence. The new model has been applied to various flow situations, even for the cases with the presence of sub-critical and supercritical flows simultaneously or sequentially. Comparisons between the numerical results and the experimental data show that the proposed model is robust with satisfactory accuracy. Copyright © 2000 John Wiley & Sons, Ltd.

KEY WORDS: boundary condition; curvilinear co-ordinate system; depth-averaged two-dimensional model; explicit–finite–analytic method

1. INTRODUCTION

A review of the literature shows that many depth-averaged numerical models have been developed and applied to free-surface flow problems. Although a depth-averaged model may suffer from some limitations on physical interpretation, e.g. invalid governing equations in the vicinity of the bore with sharp curvature, the computed results may still be used with confidence for typical engineering applications [1].

For convection-dominated open-channel flows, such as flow affected by the tidal current, circulated flow, surge, dam-break flow, or flow through abruptly varied channel sections, numerical difficulties and unsatisfactory simulated flow patterns may occur due to inadequate

* Correspondence to: Department of Civil Engineering, National Chiao Tung University, 1001 Ta Hsueh Road, Hsinchu, 30050 Taiwan, Republic of China. Fax: + 886 3 5724652.
[1] E-mail: u8316529@cc.nctu.edu.tw

Received September 1998
Revised July 1999

treatment of the non-linear convective terms. This fact is responsible for the genesis of a new generation of models, either by utilizing finite difference discretization of higher-order accuracy or by isolating the convective terms and discretizing them by different methods [2]. Chapman and Kuo [3] adopted the spatially third-order-accurate QUICK finite difference scheme to overcome the numerical problems associated with the use of upwind (first-order) and central (second-order) finite difference for the convective terms. However, the high-order-accurate schemes are usually computationally expensive. Ye and McCorquodale [4] discretized the convective terms by Roe's [5] scheme, as well as power-law scheme [6], based on the finite volume method. Roe's scheme has the advantage of computational efficiency; however, it produces better accuracy in predicting flow patterns than those from the Power-law scheme only when grids are not aligned with the currents. Benque *et al.* [2] used the method of characteristics for the convective terms, however, with the convection being treated separately in each spatial direction. Thus, two sequential one-dimensional calculations for convection of each direction were executed for a two-dimensional flow. In their paper, flow configurations in a circular basin and in a channel with the projection of spur–dike were shown. In this paper, the explicit–finite–analytic (EFA) method [7] is used to calculate the convective terms, while the other terms in the momentum equations are discretized by the finite difference method. The basic idea and also the merit of the EFA method is the incorporation of a local analytic solution in the numerical solution of a linear or linearized hyperbolic equation. The EFA method is similar to the method of characteristics because both methods bear the same characteristic line defined by the local flow velocity, referred to as the world line [8] in the method of characteristics. However, the EFA method has the advantage of simplicity and is numerically formulated from the concept of a mathematically exact solution of the equation.

Moreover, owing to the physical character of the transmission of the convection, special treatments are usually incorporated into many schemes to account for the relevant direction of transmission. For instance, (1) splitting technique: accomplished by splitting the coefficient matrices into the sub-matrices relating to positive or negative eigenvalues respectively (such as that adopted by Gabutti [9]); and (2) upwind difference: accomplished by switching the differentiating direction according to the relevant velocity components. These are usually the treatments taken. In the EFA method, it is straightforward to take the transmission character of the convection into account by the local analytic formulation of convection effect. From this point of view, the EFA method is suitable for dealing with the convective terms

In addition to the aforementioned models, Fennema and Chaudhry [10] used the Beam and Warming implicit finite difference scheme to discretize the two-dimensional unsteady free-surface equations. Molls *et al.* [11] used both the alternating direct implicit (ADI) and the MacCormack explicit schemes to simulate the two-dimensional flow near a spur–dike. It is necessary to add artificial viscosity for numerical stability in the Molls' models. Note that both Fennema and Chaudhry's and Molls *et al.*'s models partially transformed the governing equations from the physical domain to the computational domain with the adoption of orthogonal Cartesian co-ordinate grids. Moreover, Fraccarollo and Toro [12] adopted the weighted average flux method, which is a conservative shock-capturing method of Godunov type, to simulate a dam-break problem with the governing equations located in the Cartesian co-ordinate system. It can be seen that most of the existing two-dimensional models describe their governing equations in the Cartesian co-ordinate system, and a few of them are expressed

in the form of partial transformation. In this paper, the generalized governing equations are expressed in the non-orthogonal curvilinear co-ordinate system by full transformation [13], and the body-fitting grid systems are used to accurately define the geometry of the physical domain.

The aim of this paper is to propose a depth-averaged two-dimensional EFA model suitable for free-surface flows. The general formulations of the governing equations of the free-surface flows will be described first. Then the basic idea of the EFA method will be shown. Introduction of the numerical algorithm of the proposed model and the treatment of the boundary conditions will be shown in the following sections. Finally, applications and verifications of the proposed EFA method are further demonstrated via sample problems.

2. GOVERNING EQUATIONS

Incompressible flows can be formulated by describing the conservative laws of mass and momentum, and the resulting equations could be written in the tensor form as

Continuity equation:

$$V^i_{,i} = 0 \tag{1}$$

Momentum equations:

$$\frac{\partial V^i}{\partial t} + V^m V^i_{,m} = -g^{im}\frac{P_{,m}}{\rho} + \frac{\mu}{\rho} g^{mn} V^i_{,mn} - \left(\tilde{\tilde{v}^i \tilde{v}^m} \right)_{,m} + F^i \tag{2}$$

with

$$V^i_{,jk} = \frac{\partial V^i_{,j}}{\partial \xi^k} + \Gamma^i_{\alpha k} \cdot V^\alpha_{,j} - \Gamma^\alpha_{jk} \cdot V^i_{,\alpha} \tag{3}$$

$$V^i_{,j} = \frac{\partial V^i}{\partial \xi^j} + \Gamma^i_{\alpha j} V^\alpha, \qquad P_{,j} = \frac{\partial P}{\partial \xi^j} \tag{4}$$

$$\Gamma^i_{jk} = \frac{1}{2} g^{il} \cdot \left(\frac{\partial g_{lk}}{\partial \xi^j} + \frac{\partial g_{lj}}{\partial \xi^k} - \frac{\partial g_{jk}}{\partial \xi^l} \right) \tag{5}$$

$$g_{ij} = \frac{\partial \tilde{r}}{\partial \xi^i} \cdot \frac{\partial \tilde{r}}{\partial \xi^j}, \qquad g^{ij} = \nabla \xi^i \cdot \nabla \xi^j \tag{6}$$

(all sub-ordinate indices = 1, 2, 3) in which ρ is the density of fluid; P is the pressure; g^{mn} and g_{mn} are contravariant and covariant metric tensors respectively; μ is the dynamic viscosity of fluid; F is the body force vector; t is the time; and $\tilde{r}$ is the position vector. The mark $\tilde{\tilde{\ }}$ represents the ensemble averaging procedure. In Equations (1)–(6), all repeated sub-ordinate

indices in one term are dummy indices. Moreover, the V^i and v^i are mean and fluctuating contravariant velocity components respectively, tangent to the ξ^i co-ordinate axis, and their quantities are measured by the scale of dependent co-ordinate system. Therefore, in order to obtain the physical quantities $V(i)$ and $v(i)$, the V^i and v^i are multiplied by the metric coefficients as

$$V(i) = g_{ii}^{0.5} \cdot V^i, \qquad v(i) = g_{ii}^{0.5} \cdot v^i \quad \text{(no summation over } i\text{)} \tag{7}$$

With the general convention $[V(1), V(2), V(3)] = (u, v, w)$ and $[v(1), v(2), v(3)] = (u', v', w')$ are the physical mean and fluctuating velocity components in the (ξ, η, ζ) co-ordinate directions respectively. One can obtain the two-dimensional depth-averaged shallow-water equations by integrating Equations (1) and (2) along the water depth with the following assumptions:

1. The surface wind shear stress and the Coriolis acceleration are assumed to be negligible.
2. The channel bed slope is small, which leads to $g_{13} = g_{23} = 0$, $g^{13} = g^{23} = 0$, and the metric tensors in the vertical direction equal one, i.e. $g_{33} = g^{33} = 1$.
3. The vertical velocity component w is negligible. Hence, the momentum equation in the vertical direction simplifies into the equation of hydrostatic pressure distribution, such that the pressure P could be replaced by water depth.
4. The power-law velocity distribution over the depth is assumed in both the ξ- and η-directions:

$$u = \frac{N+1}{N}\bar{u}\left(\frac{\delta}{h}\right)^{1/N}, \qquad v = \frac{N+1}{N}\bar{v}\left(\frac{\delta}{h}\right)^{1/N} \tag{8}$$

in which $\bar{u}$ and $\bar{v}$ are depth-averaged velocities in the ξ- and η-directions respectively; δ is the distance from the channel bed; h is the water depth; and $N = \kappa\sqrt{8/f}$, in which κ is the von Karman coefficient and f is the Darcy–Weisbach coefficient.

The effective stresses, as defined by Kuipers and Vreugdenhil [14], including laminar viscous, turbulent Reynolds and dispersive stresses, are all considered in the proposed EFA model. It may be noted that the dispersive stresses result from a concurrence of depth integration procedures of non-linear convective terms and the existing non-uniform distribution of the velocity profile over the depth. Yet these dispersive stresses are usually not taken into account in the existing models, such as those of Tingsanchali and Maheswaran [15], Bhallamudi and Chaudhry [16] and Fraccarollo and Toro, under the assumption of uniform velocity distribution over the depth. In the proposed EFA model, the power-law velocity distribution over the depth has been assumed; hence the dispersive stresses were considered. On the other hand, the Boussinesq's [17] eddy viscosity concept is adopted for the expression of the turbulent Reynolds stresses

$$\tilde{}\,\tilde{}\,\tilde{v^i}\tilde{v^j}\,\tilde{}\,\tilde{} = \nu_t(V^i_{,j} + V^j_{,i}) \tag{9}$$

and the eddy viscosity can be determined as

$$v_t = \frac{\kappa u_* h}{6} \tag{10}$$

in which u_* is the shear velocity [18].

The bed frictions in the ξ- and η-directions are determined in accordance with the following:

$$\tau_{b\xi} = \frac{\rho g}{C^2} V_\xi \cdot |V|, \quad V_\xi = \bar{u} + \bar{v} g_{11}^{-0.5} g_{22}^{-0.5} g_{12} \tag{11a}$$

$$\tau_{b\eta} = \frac{\rho g}{C^2} V_\eta \cdot |V|, \quad V_\eta = \bar{v} + \bar{u} g_{11}^{-0.5} g_{22}^{-0.5} g_{12} \tag{11b}$$

and

$$|V| = [\bar{u}^2 + \bar{v}^2 + 2\bar{u}\bar{v} g_{11}^{-0.5} g_{22}^{-0.5} g_{12}]^{0.5} \tag{12}$$

in which g is the gravitational acceleration; C is the Chezy coefficient; V_ξ and V_η are the factual magnitudes of velocity components in the ξ- and η-directions respectively (note that they are slightly different from $\bar{u}$ and $\bar{v}$ as they are located in the non-orthogonal co-ordinate system); and $|V|$ is the magnitude of the velocity vector. Derivation of the depth-averaged two-dimensional shallow-water equations in the general curvilinear co-ordinate system is involved and hence not dealt here. Only the final forms of the depth-averaged continuity and momentum equations are listed in Appendix A. These equations can be rewritten in the compact forms as following:

Continuity equation:

$$\frac{\partial h}{\partial t} + g_{11}^{-0.5} g_{22}^{-0.5} \frac{\partial [g_{22}^{0.5} \cdot \bar{u} h]}{\partial \xi} + g_{11}^{-0.5} g_{22}^{-0.5} \frac{\partial [g_{11}^{0.5} \cdot \bar{v} h]}{\partial \eta} + C_1 \cdot \bar{u} h + C_2 \cdot \bar{v} h = 0 \tag{13}$$

Momentum equations:

$$\frac{\mathrm{D}V(i)}{\mathrm{D}t} = S_\mathrm{d} + S_\mathrm{p} + S_\mathrm{f} + S_\mathrm{t} + S_\mathrm{c}, \quad i = 1, 2 \tag{14}$$

in which

$$\frac{\mathrm{D}V(i)}{\mathrm{D}t} = \frac{\partial V(i)}{\partial t} + g_{ii}^{0.5} \cdot V^m V^i_{,m} \quad \text{(summation over } m\text{)} \tag{15}$$

in which C_1 and C_2 are metric coefficients, $\mathrm{D}/\mathrm{D}t$ is the total derivative with respect to time, S_d is the dispersion term resulting from the depth integration of the non-linear convective accelerations, S_p is the propagation term associated with the hydrostatic pressure, S_f is the friction term resulting from the solid boundaries, S_t is the turbulence term, and S_c is the collection of residuals including the laminar viscosity term.

3. CO-ORDINATE AND GRID SYSTEM

To properly define the irregular boundaries, especially those of the natural rivers, body-fitted grid systems are preferable to the Cartesian grid systems in the finite difference method. It may be noted that the calculated flux adjacent to a corner might be incorrect when the computation is executed in a Cartesian grid system [15,19]. The use of a body-fitted grid system has the advantage of avoiding this kind of error. Two different approaches, partial and full transformations of the governing equations to the general co-ordinate systems, facilitate the equations to be solved on the body-fitted grid systems. By partial transformation, it is only a mapping between two different co-ordinate systems, leaving the dependent velocity components in the original x- and y-directions. This approach has the advantage of relative simplicity, however, it may lead to increased numerical diffusion due to large skew angles between the velocity components and the faces of the computational cell [13] or large discrepancies between the directions of velocity components and co-ordinate axes. Alternatively, by full transformation, the dependent velocity components direct along the curvilinear co-ordinate axes, i.e. along the ξ- and η-directions, rather than along the x- and y- directions, avoiding the above discrepancy problem. Hence, in this paper, full transformation is adopted to derive the two-dimensional depth-averaged shallow-water equations in the general curvilinear co-ordinate system, as it is suitable for carrying out the computation in the body-fitted grid systems.

On the other hand, though grid generation methods attempt to maintain mutually perpendicular co-ordinate axes, numerically established structural grid systems do not guarantee their orthogonality, especially in the place where the geometry is complex or has sharp curvature. If orthogonal governing equations are solved on a non-orthogonal grid system, numerical errors may occur due to the inconsistency. Therefore, adoption of non-orthogonal governing equations is suitable for flow with complex boundaries. It may be recalled that the governing equations (13) and (14) are written in the general curvilinear co-ordinate system by full transformation, and conserve the inner dot products g_{12} and g^{12} to take account of the effect of using non-orthogonal grids.

4. EXPLICIT–FINITE–ANALYTIC METHOD

The EFA method finds the local analytic solutions of convection part of momentum equations on each nodal point within a local element. The basic concept of the EFA method can be explained by solving the two-dimensional first-order linear hyperbolic equation without source terms written in the Cartesian co-ordinate system

$$\phi_t + u\phi_x + v\phi_y = 0 \tag{16}$$

in which u and v are velocities in the x- and y-directions respectively and are regarded as constants. If the initial condition is properly specified, Equation (16) can be solved analytically. Under the initial condition $\phi(x, y, 0) = \varphi(x, y)$, the analytic solution, after marching a time step Δt from the initiation, can be expressed as

$$\phi(x_0, y_0, \Delta t) = \varphi(x_0 - u\Delta t, y_0 - v\Delta t) \tag{17}$$

in which (x_0, y_0) is the location on which ϕ is to be solved, and $x = x_0 - u\Delta t$ and $y = y_0 - v\Delta t$ define a characteristic line projecting from the initial plane to the position (x_0, y_0) at Δt time plane. For purely convective phenomena, it can be recognized that the adoption of the upwind direction is intuitive and straightforward. For example, as u and v are both positive in the conventional co-ordinate system (Figure 1), the flow comes from the southwest, inducing that the characteristic line projects from the southwest to the northeast and intersects the initial plane at a point southwest of (x_0, y_0). Similarly, different combinations of the signs of u and v represent the different directions of convection, and the directions can be automatically adjusted by Equation (17) to obtain the correct convective information.

As for the momentum equations of open-channel flows, non-linearity of the convective terms makes it impossible to obtain an analytic solution for the entire flow field. In this paper, the non-linear convection terms are locally linearized by simply substituting the constant representative velocities for the convective velocities, called the characteristic velocities hereafter, e.g. u and v in Equation (16), so that the local analytic solutions may be determined on the individual discretized nodal points as described above. Although the convective velocities vary with space and time, the constant characteristic velocities could be used for representing the average convective feature in a local cell element during a small time step. The remaining problem is to determine the appropriate characteristic velocities for each local cell element.

As for the non-homogeneous equation, e.g. Equation (14), the right-hand side terms could be simply differentiated with known variables and integrated over the time step. The results are treated as the source terms and added to the convective quantity in the right-hand side of the Equation (17). This is the overall algorithm of Dai's [7] EFA method to determine the solution explicitly. His model was applied to cavity flows without free surface. In this paper, an iterative procedure is used to update the known variables, the source terms and the characteristic velocities.

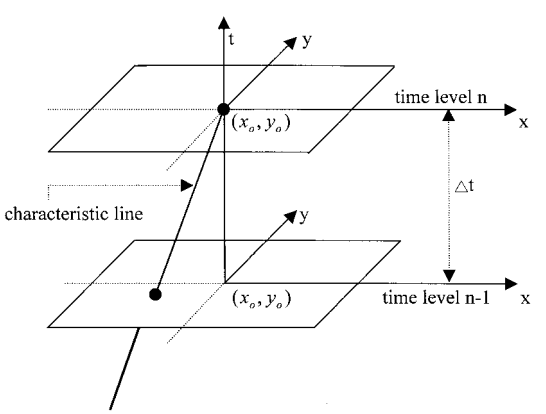

Figure 1. Definition sketch of characteristics line for EFA method.

5. NUMERICAL ALGORITHM

In the proposed model, the convective parts of the momentum equations are solved by the EFA method, but the remainders, as well as the continuity equation, are solved by the finite difference method. The flow velocities and water depth to be solved are located on staggered nodal points as shown in Figure 2. An iterative procedure is taken to make the flow variables reach convergence simultaneously during each time step. The discretized governing equations are as follows:

$$h_{i,j}^{n+1} = h_{i,j}^{n} + \left\{ \begin{array}{c} \theta \cdot [g_{11}^{-0.5} g_{22}^{-0.5} \cdot [\nabla_\xi \Delta_\xi (g_{22}^{0.5} \cdot \bar{u}h) + \nabla_\eta \Delta_\eta (g_{11}^{0.5} \cdot \bar{v}h)] + C_1 \cdot \bar{u}h + C_2 \cdot \bar{v}h]_{i,j}^{n+1*} \\ + (1-\theta) \cdot [g_{11}^{-0.5} g_{22}^{-0.5} \cdot [\nabla_\xi \Delta_\xi (g_{22}^{0.5} \cdot \bar{u}h) + \nabla_\eta \Delta_\eta (g_{11}^{0.5} \cdot \bar{v}h)] + C_1 \cdot \bar{u}h + C_2 \cdot \bar{v}h]\}_{i,j}^{n} \end{array} \right\} \cdot \Delta t \tag{18}$$

$$\bar{u}_{i-1,j}^{n+1} = \bar{u}_{\mathrm{con}} + \left\{ \begin{array}{c} \theta \cdot [S_{\mathrm{d}} + S_{\mathrm{p}} + S_{\mathrm{f}} + S_{\mathrm{t}} + S_{\mathrm{c}}]_{i-1,j}^{n+1*} \\ + (1-\theta) \cdot [S_{\mathrm{d}} + S_{\mathrm{p}} + S_{\mathrm{f}} + S_{\mathrm{t}} + S_{\mathrm{c}}]_{i-1,j}^{n} \end{array} \right\} \cdot \Delta t \tag{19}$$

$$\bar{v}_{i,j-1}^{n+1} = \bar{v}_{\mathrm{con}} + \left\{ \begin{array}{c} \theta \cdot [S_{\mathrm{d}} + S_{\mathrm{p}} + S_{\mathrm{f}} + S_{\mathrm{t}} + S_{\mathrm{c}}]_{i,j-1}^{n+1*} \\ + (1-\theta) \cdot [S_{\mathrm{d}} + S_{\mathrm{p}} + S_{\mathrm{f}} + S_{\mathrm{t}} + S_{\mathrm{c}}]_{i,j-1}^{n} \end{array} \right\} \cdot \Delta t \tag{20}$$

in which $\nabla_\xi \Delta_\xi$ and $\nabla_\eta \Delta_\eta$ indicate the central differences in the ξ- and η-directions respectively; subscripts i and j define the grid points; subscript 'con' defines the location from which flow information is transferred to the current computed point by convection; superscripts n and $n+1$ indicate the previous and present time levels respectively; superscript $n+1*$ indicates the newly updated quantities from the previous iteration. It may be noted that variables marked with superscript $n+1*$ are equivalent to those marked with n for the first iteration of each time step and are updated subsequently by the newly calculated quantities of the current time. Besides, owing to the time dependence, variables marked with n and $n+1*$ are weighted by a factor θ to substitute for integration over a time step. To determine the convective information of $\bar{u}_{\mathrm{con}}$ and $\bar{v}_{\mathrm{con}}$, it requires appropriate characteristic velocities, i.e. u and v in Equation (17),

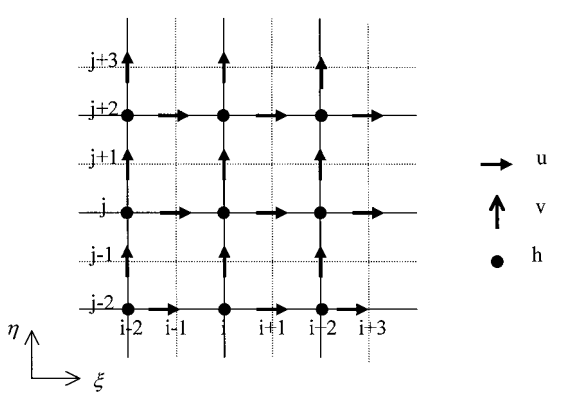

Figure 2. Computational grids.

to trace back to the location at which the characteristic line intersects the previous time level. By numerical experience, the newly calculated velocities are appropriate to be the characteristic velocities. For example, the characteristic velocities $(u, v) = (\bar{u}_{i-1,j}^{n+1*}, \bar{v}_{i-1,j}^{n+1*})$ are used to determine $\bar{u}_{\text{con}}$ in Equation (19) for the characteristic line passing through the point $(i-1, j)$ at the current time level. Similarly, the characteristic velocities $(u, v) = (\bar{u}_{i,j-1}^{n+1*}, \bar{v}_{i,j-1}^{n+1*})$ are adopted for the determination of $\bar{v}_{\text{con}}$ in Equation (20). On the other hand, the initial condition $\varphi(x, y)$ at the n time step can be established by a bilinear method for irregular two-dimensional meshes [20] with the known variables at four vertices of the cell involving the location 'con'.

Note that the characteristic velocities are in the directions consistent with the curvilinear co-ordinate axes. To define the location at which the characteristic line intersects the previous time level, i.e. $(x_0 - u\Delta t, y_0 - v\Delta t)$, the characteristic velocities are transformed to the Cartesian co-ordinate system. The characteristic velocities in the Cartesian and curvilinear co-ordinate systems have the following relationships:

$$\bar{u}_{\text{car}} = \bar{u}_{\text{cur}} \cdot g_{11}^{-0.5} \frac{\partial x}{\partial \xi} + \bar{v}_{\text{cur}} \cdot g_{22}^{-0.5} \frac{\partial x}{\partial \eta} \tag{21}$$

$$\bar{v}_{\text{car}} = \bar{u}_{\text{cur}} \cdot g_{11}^{-0.5} \frac{\partial y}{\partial \xi} + \bar{v}_{\text{cur}} \cdot g_{22}^{-0.5} \frac{\partial y}{\partial \eta} \tag{22}$$

where subscripts 'car' and 'cur' denote the velocities in the Cartesian and curvilinear co-ordinate systems respectively. Then $\bar{u}_{\text{con}}$ and $\bar{v}_{\text{con}}$ can be determined by Equation (17).

For free-surface flows, the direction of disturbance propagation depends on whether the flow is sub-critical or supercritical. For sub-critical flows, disturbance propagates both in the upstream and downstream directions. On the other hand, for supercritical flows, disturbance propagates either upstream or downstream depending on the flowing direction. Therefore, the source terms, including S_{d}, S_{p} and S_{c}, in the momentum equations in the proposed model are differentiated using central difference for sub-critical flow, and upwind difference for supercritical flow.

The right-hand side of Equations (18)–(20) may be calculated explicitly with known variables, consequently obtaining the new flow situation at the present time level explicitly. The algorithm can be summarized as follows:

1. Compute $\bar{u}^{n+1}$ and $\bar{v}^{n+1}$ by Equations (19) and (20) respectively on the staggered nodal points.
2. Compute h^{n+1} by Equation (18) on the main nodal points with newly calculated velocities from step 1.
3. Update the characteristic velocities and use the newly calculated variables to repeat steps 1–3 until the convergent criteria are met.
4. March to the next time step and repeat steps 1–4 until the steady state or the end of simulation period is reached.

The proposed model can be applied to both for steady and unsteady free-surface flows. When a steady flow is simulated, time marching is repeated as that for unsteady flow until the flow variables at successive time steps have negligible difference.

6. NUMERICAL ACCURACY AND STABILITY OF THE MODEL

The analysis of truncation error by Taylor's series expansion shows that the accuracy of the proposed model is second-order in space and first-order in time [7]. However, as the upwind difference, which is first-order accurate in space, is adopted for source terms in the momentum equations to account for the nature of flow *viz*. supercritical flow as described earlier, the overall accuracy in space will be dominated by the upwind difference.

Similar to other explicit numerical models, the Courant–Friedrichs–Lewy (CFL) condition is the constraint of choosing the marching time step. The CFL condition is given by

$$Cr_{\xi} = \frac{(|\bar{u}| + c)\cdot \Delta t}{\Delta \xi \cdot g_{11}^{0.5}} \leq 1 \tag{23}$$

$$Cr_{\eta} = \frac{(|\bar{v}| + c)\cdot \Delta t}{\Delta \eta \cdot g_{22}^{0.5}} \leq 1 \tag{24}$$

where c is the wave celerity of the free-surface flow, and is defined as $\sqrt{gh}$; Cr is the Courant number. When the determination of the time step is based on these two inequalities, the characteristic lines associated with Equations (19) and (20) can be ensured to pass through the local element as shown in Figure 1.

7. BOUNDARY CONDITIONS

It has been noted that the only general technique available for dealing with the boundary conditions is the method of characteristics [21]. For two-dimensional flows, it prefers to locate the upstream and downstream boundaries at sections where cross-stream flux is insignificant so that almost unidirectional (in the ξ-direction) flow enters or leaves the simulated region. Under such a situation, the characteristic equations describing the propagation of disturbances mainly along the streamline direction can be used for approximating the boundary conditions. There are three of the characteristic equations individually processing the characteristic velocity vectors of $(\bar{u} + c, \bar{v})$, $(\bar{u} - c, \bar{v})$ and $(\bar{u}, \bar{v})$. The three characteristics may direct toward upstream or downstream, depending on the flow pattern. As an illustration, for flow with positive $\bar{u}$, $(\bar{u} + c, \bar{v})$ and $(\bar{u}, \bar{v})$ direct downstream, yet $(\bar{u} - c, \bar{v})$ directs upstream in the sub-critical flow regime; whereas all of them direct downstream in the supercritical flow

regime. Therefore, it necessitates different alternatives to deal with the boundary conditions under different flow situations.

For sub-critical flow cases, two boundary conditions related to discharge hydrographs per unit width $q_\xi(t)$ and $q_\eta(t)$ in the ξ- and η-directions respectively are specified at the upstream boundary because two of the three characteristic lines related to velocity vectors $(\bar{u}+c, \bar{v})$ and $(\bar{u}, \bar{v})$ are obtained from the outside of the computational region. Thus, the water depth can be approximated by the characteristic equation as

$$\frac{c}{h}\frac{\mathrm{d}h}{\mathrm{d}t} - \frac{\mathrm{d}\bar{u}}{\mathrm{d}t} + g_{22}^{-0.5} c \frac{\partial \bar{v}}{\partial \eta} = -g(S_{0\xi} - S_{\mathrm{f}\xi}) \tag{25}$$

in which $\mathrm{d}/\mathrm{d}t$ denotes characteristic lines projecting along with velocity vector $(\bar{u}-c, \bar{v})$. Note that $S_{0\xi}$ and $S_{\mathrm{f}\xi}$ are the bed and friction slopes along the ξ-direction respectively. Similarly, one boundary condition related to $h(t)$ is required at the downstream boundary as the characteristic line related to $(\bar{u}-c, \bar{v})$ is obtained from outside. Thus, the remaining two unknowns, i.e. q_ξ and $\bar{v}$, can be approximated by the characteristic equations as

$$\frac{\mathrm{d}q_\xi}{\mathrm{d}t} + (c-\bar{u})\frac{\mathrm{d}h}{\mathrm{d}t} = gh(S_{0\xi} - S_{\mathrm{f}\xi}) - g_{22}^{-0.5} ch \frac{\partial \bar{v}}{\partial \eta} \tag{26}$$

$$\frac{\delta \bar{v}}{\delta t} + g_{22}^{-0.5} g \frac{\partial h}{\partial \eta} = g(S_{0\eta} - S_{\mathrm{f}\eta}) \tag{27}$$

in which $\mathrm{d}/\mathrm{d}t$ and $\delta/\delta t$ denote characteristic lines projecting along with velocity vectors $(\bar{u}+c, \bar{v})$ and $(\bar{u}, \bar{v})$ respectively; $S_{0\eta}$ and $S_{\mathrm{f}\eta}$ are bed and friction slopes along the η-direction respectively. On the other hand, three boundary conditions are required at the upstream boundary for supercritical flow cases because all the three characteristic lines are from outside, and Equations (25)–(27) are used to approximate the flow pattern at the downstream boundary.

The algorithm for solving the open boundary conditions is similar to that for computing flow variables at the interior grid points. No-slip condition and null normal flux are specified at the solid walls, and the water surface elevations along the walls are extrapolated from those at the nearby interior points.

8. APPLICATIONS

To demonstrate the applicability of the proposed EFA model, different flow examples are simulated. Sub-critical and supercritical flows may exist simultaneously in different locations or in sequence in time, such as the hydraulic jump and dam-break wave with a sharp discontinuity of the water surfaces. Such complex flow patterns make many of the existing schemes fail. In this paper, several test cases possessing this feature of mixed flow types are simulated to demonstrate the capability of the proposed model. The numerical results from the

proposed model are verified by the already existing experimental data, and are compared with that from other models. All the simulations start with generating the grid systems and only the resulting computational grids are shown. To ensure numerical stability for each test case, Equations (23) and (24) are used to determine Δt for each time marching step.

8.1. Jet circulation in circular basin

The geometry of the circular basin with diametrically opposite inlet and outlet [18] is shown in Figure 3. The radius of the basin is 0.75 m; the inlet is of 0.08 m in width and length; the outlet is 0.24 m in width and 0.1 m in length; and all have vertical side walls. The bottom is flat and the Chezy frictional coefficient is set to be $45\,m^{0.5}\,s^{-1}$. The inflow discharge is $0.01\,m^3\,s^{-1}\,m^{-1}$, and a fixed depth of 0.09 m is specified at the outlet in the simulation. Jet flow through the circular basin involves flow separation and circulation. This layout of the basin is a suitable case to test the EFA model for its ability to handle the non-linearly convective acceleration of the flow. The body-fitted grid system for numerical simulation is also shown in Figure 3. It can be seen that the circular boundary is well defined by the body-fitted co-ordinate system. The whole domain is discretized into (41×23) grid points. The grid system cannot maintain orthogonality, especially at the interfaces of the inlet/outlet and the circular basin. Therefore, the use of non-orthogonal governing equations for problem solving is necessary.

The importance of the non-linearly convective accelerations and viscous terms for simulating flows with separation and circulation has already been pointed out by Falconer [18] and Ponce and Yabusaki [22] and has been verified by Benque *et al.* Recently, Borthwick and Akponasa

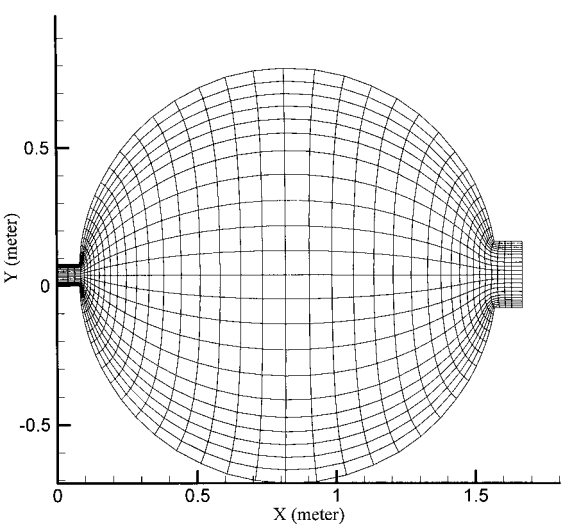

Figure 3. Computational grids for jet flow simulation.

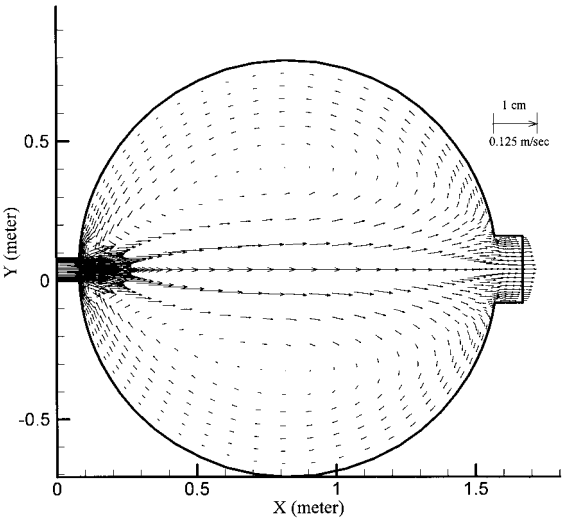

Figure 4. Velocity vectors of jet flow circulation obtained using EFA model.

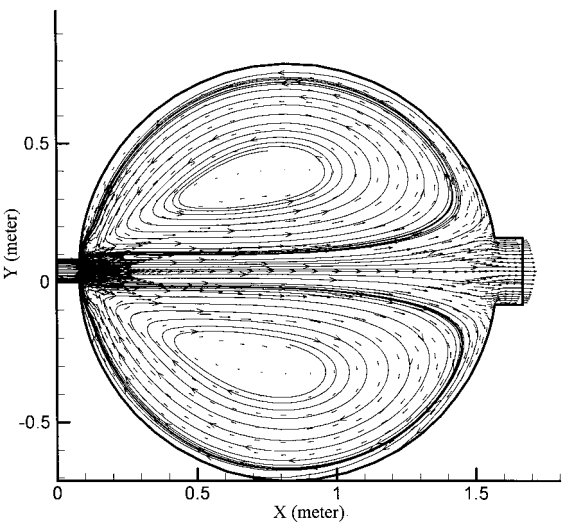

Figure 5. Streamlines of jet flow.

[23] simulated flow patterns in basins with the similar shape as shown in Figure 3. The steady velocity distributions for different inlet Reynolds numbers were given by Akponasa [23]; however, unreasonably exaggerated velocity vectors near the outlet could be seen in their paper

[23]. Figure 4 shows the distribution of the velocity vectors by the proposed model. It can be seen that no unreasonably exaggerated velocity vectors appear and the fluid flows outside the basin smoothly. The separation and circulation of the flow in the basin can be clearly seen from the corresponding streamline as shown in Figure 5. At the beginning of the jet flow entering the basin, the momentum is largely maintained in the jet direction with a little lateral spread. Because of the viscous effects, fluid on both sides of the jet in the basin is impelled and the circulation intensity gradually increases. Figure 6 shows the final contours in the equilibrium state. The minimum depth occurs around the upstream center part of the basin and the maximum depth occurs around the downstream sides of the basin. The simulated results demonstrate the capability of the EFA model for dealing with convection-dominated flows.

8.2. Hydraulic jump

Hydraulic engineers are concerned with the location and the conjugated water depths of a hydraulic jump. Rahman and Chaudhry [24] have used two different numerical schemes, MacCormack and two–four, to simulate the hydraulic jump for different Froude numbers. They added the Boussinesq terms into St. Venant equations to account for the non-hydrostatic pressure distribution in the region of steep gradients of depth and velocity, and then used the resulting Boussinesq equations to simulate the hydraulic jump. Their simulated results agreed well with the experiments conducted by Gharangik and Chaudhry [25]. They also found the Boussinesq terms to be very small relative to other terms. This finding led to the conclusion that the inclusion of the Boussinesq terms is not important. Hence, although the

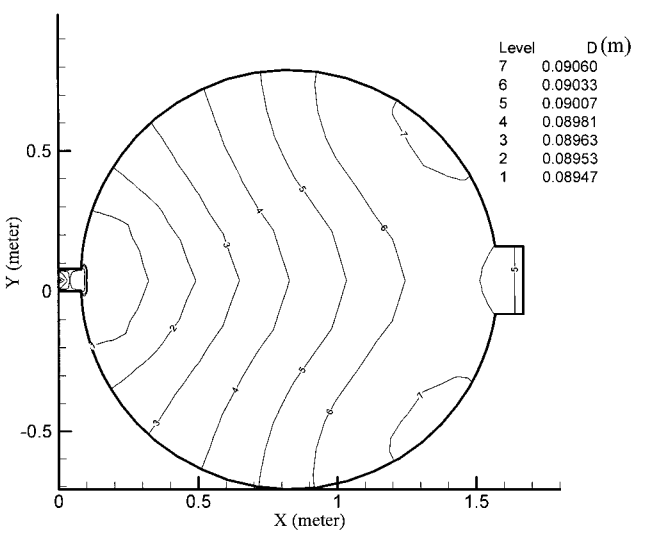

Figure 6. Contours of jet flow.

depth-averaged model suffers from the shortcoming of invalidating governing equations in the vicinity of the bore with sharp curvature of water surface, it can still be used with confidence for practical applications.

In Rahman and Chaudhry's models, artificial viscosity is required to dampen the high-frequency oscillations near the steep gradient. Moreover, additional parameters were introduced into their models to regulate the amount of artificial viscosity. Using excessive artificial viscosity may introduce numerical dispersion. Therefore, for different flow situations, the magnitudes of these parameters need to be calibrated to reach a compromise between the oscillations suppressing and numerical dispersion. From the practical point of view, this may lead to some difficulties in application. In this paper, the hydraulic jump is simulated without any artificial viscosity.

Before making the numerical simulation possible, further investigation on the hydraulic jump is necessary. In the supercritical flow region, three boundary conditions are needed at the upstream end. However, one additional internal boundary condition associated with the hydraulic jump character is naturally induced at the interface of the two different flow regimes. Therefore, there are four boundary conditions in the supercritical flow region, and this leads to an overdetermined problem from the mathematical viewpoint. To solve this problem, the water surface elevation at the downstream end of the supercritical flow region is calculated by extrapolation from the corresponding values at adjacent upstream interior points. With this treatment, the internal boundary condition for the supercritical flow region can be eliminated. The location of the downstream end of the supercritical flow region could be defined as where the Froude number is larger than one and that of its next grid point is less than one. During each iterative procedure, Froude numbers at grid points are calculated for determining the location of the hydraulic jump.

The experimental data of Gharangik and Chaudhry are used to verify the proposed model. Data of four experimental results based on the inflow Froude number are listed in Table I. The rectangular straight channel is of 9 m in length with flat bottom. The flow domain is discretized into (61×7) grid points. The Chezy frictional coefficient was set at $30\ m^{0.5}\ s^{-1}$. For each case, the water depth and velocities in both ξ- and η-directions at the upstream boundary and water depth at the downstream boundary were specified and remained unchanged. At the beginning of the simulation, the initial flow condition throughout the channel was set as the supercritical flow pattern like that at the upstream boundary. After the depth at the downstream boundary rises, the transition of the supercritical flow to sub-critical flow starts at the downstream end and then moves toward upstream until the equilibrium is achieved. The

Table I. Test conditions for hydraulic jump (after Gharangik and Chaudhry [25]).

Froude number $u/\sqrt{gh}$	Upstream u ($m\ s^{-1}$)	Upstream v ($m\ s^{-1}$)	Upstream depth (m)	Downstream depth (m)
7.0	3.831	0.0	0.031	0.265
6.65	3.255	0.0	0.024	0.195
2.9	2.127	0.0	0.055	0.189
2.3	1.826	0.0	0.064	0.168

comparisons between the numerical results and the experimental data according the depth profile along the centerline of the channel are shown in Figures 7–10. Because of the straight channel, there is no variation across the channel except the transitions to no-slip condition at the wall. It can be seen in these figures that the proposed model well simulates both the location and conjugate depths of the jump. No matter the magnitudes of the Froude number

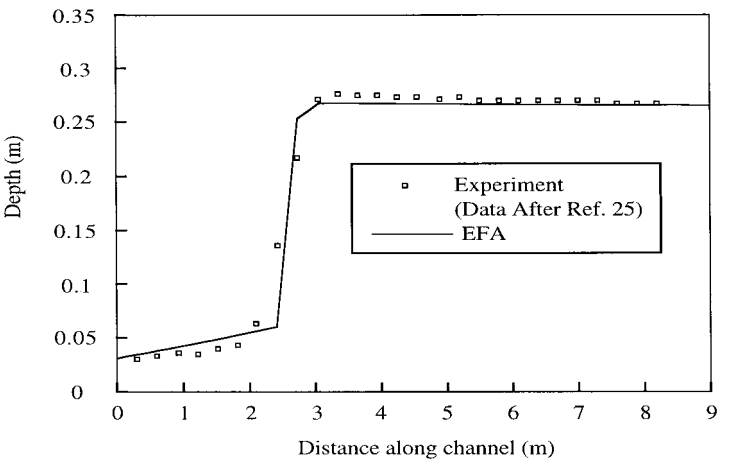

Figure 7. Jump profile for $Fr = 7.0$.

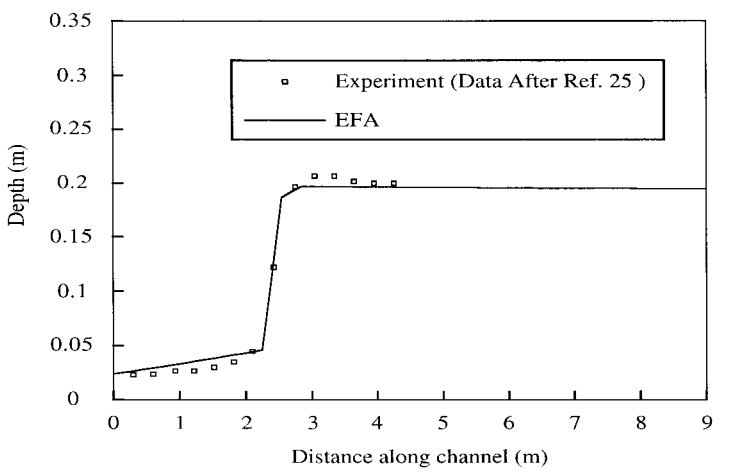

Figure 8. Jump profile for $Fr = 6.65$.

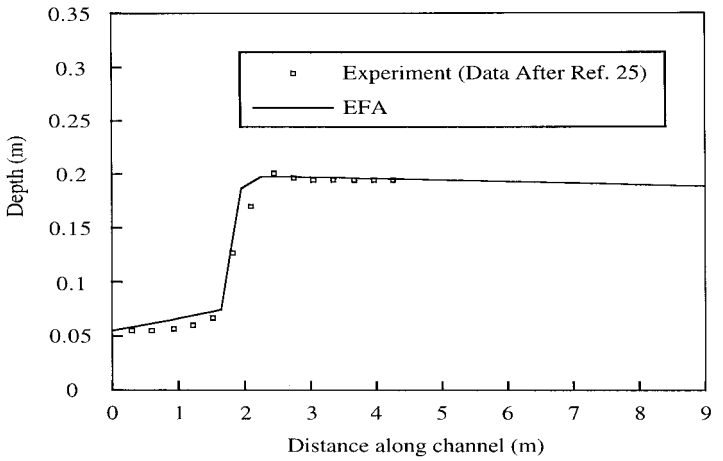

Figure 9. Jump profile for $Fr = 2.9$.

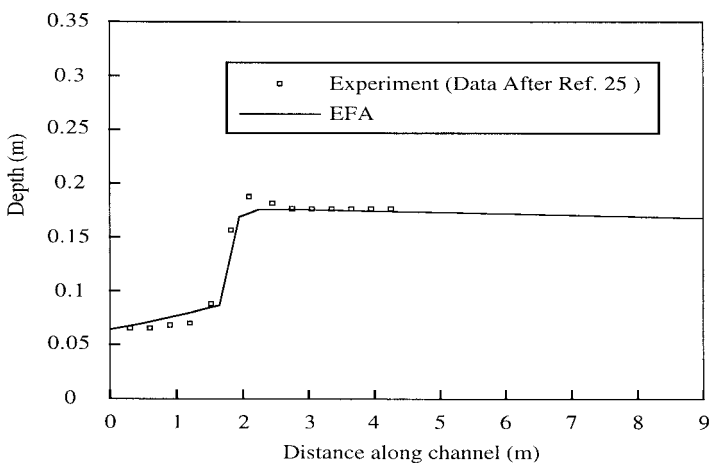

Figure 10. Jump profile for $Fr = 2.3$.

might be, numerical oscillation does not occur in each case. These test cases show that the EFA model has the capability of dealing with flows with the presence of sub-critical and supercritical regimes simultaneously or sequentially.

8.3. Dam-break flow

It is common to regard the dam-break wave as an unsteady shallow water flow [8,26]. When a dam breaches, a positive steep-front wave develops and propagates downstream, associated with a negative wave propagating oppositely upstream of the dam. The flow is usually sub-critical upstream of the dam site and is supercritical downstream. The numerical schemes used for solving the problem will face severe challenges especially when they are applied to cases with large initial water depth in the reservoir and small depth in the downstream channel. Furthermore, the extreme condition of downstream dry bed may be the case so that it needs a more robust model to deal with the problem.

Several experiments conducted by Bellos *et al.* [27] were simulated by using this model. Simulated results for only two cases are presented and compared with the experimental data, along with the results from the MacCormack method. The channel with vertical walls is 21.2 m in length and 1.4 m in width at both ends. The channel has a narrowest section in the middle reach with the width of 0.6 m there. The gate is located at the narrowest section, i.e. 8.5 m from the upstream end, and is removed instantaneously. The geometry of the experimental channel as well as the computational grids (81×15) are shown in Figure 11. The Manning coefficient is assumed as 0.012. Two cases with different bed slopes of 0.004 and 0.006 respectively were simulated. For both the cases, the initial water depth just behind the dam is 0.15 m, and the downstream channel is dry. During simulation, the water depth hydrographs along the centerline of the channel were recorded at four spots, i.e. 0, 4.5, 11 and 18.5 m respectively from the upstream end. Note that the former two spots are upstream of the dam site. The total simulation time is 65 s after the dam break.

Figure 12(a)–(d) shows the comparisons of water depth hydrographs between the numerical results and the experimental data at different measurement points for the case with bed slope of 0.004. It can be seen in Figure 12(a) and (b) that, after a period of rapid drop of the water surface, the water depth experiences a period of mild decrease or even remains unchanged.

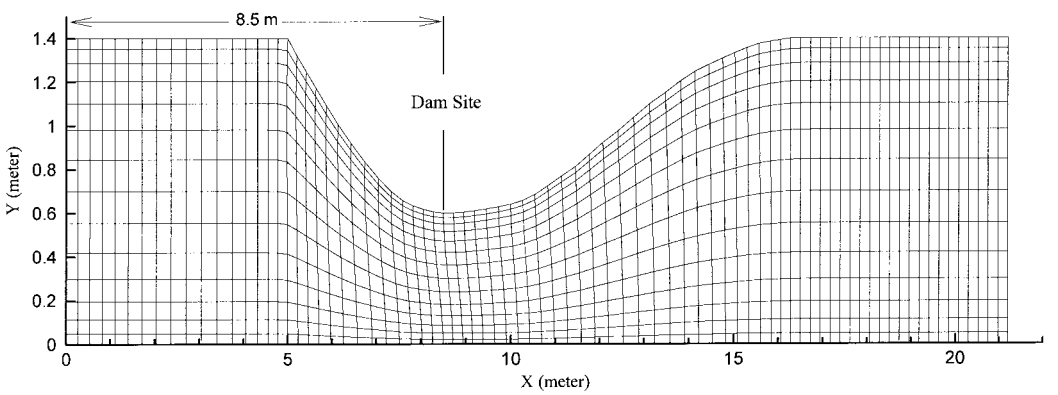

Figure 11. Computational grids for dam-break simulation.

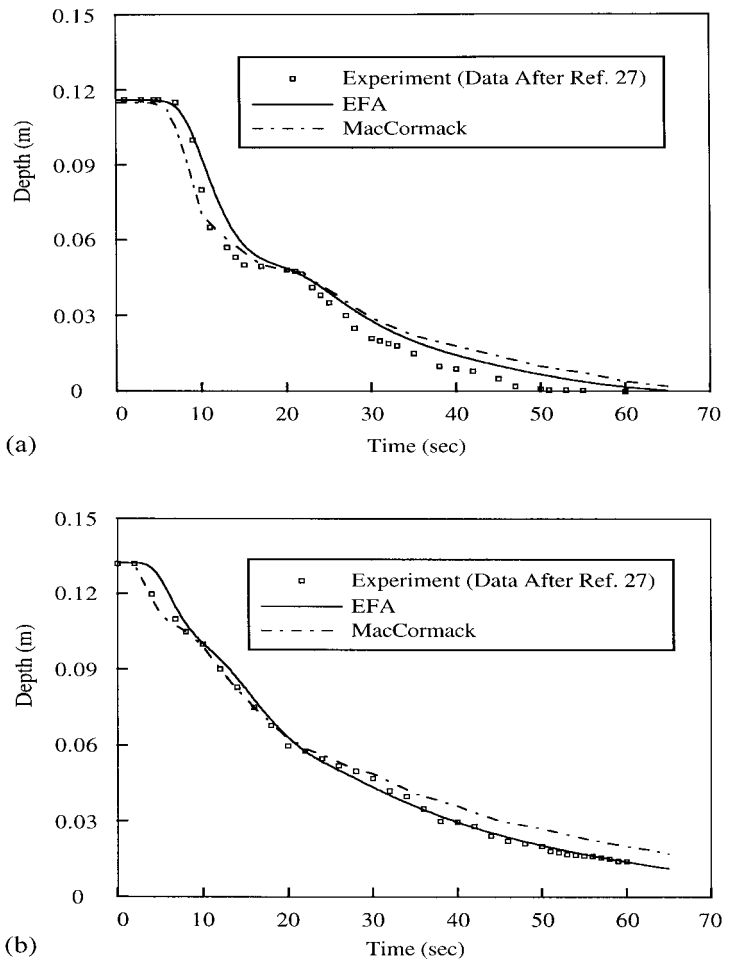

Figure 12. Comparison between computational and experimental depth hydrographs for slope = 0.004; (a) $X = 0$ m, (b) $X = 4.5$ m, (c) $X = 11$ m, (d) $X = 18.5$ m.

This phenomenon is due to the converging–diverging variation of the channel cross-section. In Figure 12(c) and (d), the simulated arrival time and wave front height are satisfactory as compared with the measured data.

Similarly, Figure 13(a)–(d) shows the comparisons for the case with bed slope of 0.006. Owing to the steeper slope, the fluid gets released to downstream channel more rapidly. From Figure 13(a), the fluid at the upstream boundary is exhausted in about 40 s after the dam break. Starting from the upstream end, the reservoir bed gradually becomes dry. The effect of the cross-sectional variation can also be seen in Figure 13(a) and (b). For the depth

hydrographs in the downstream channel, as can be seen from Figure 13(c) and (d), there exists a little protuberance resulting from numerical treatment of the discontinuously leading edge travelling on the dry bed. However, the overall results are satisfactory.

This application study demonstrates the capability of the EFA model to deal with the mixed type of unsteady sub-critical and supercritical flows and the channel bed being alternatively wet and dry.

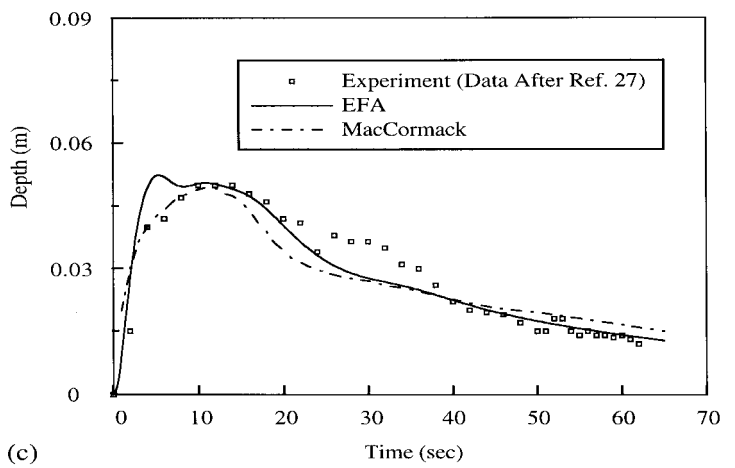

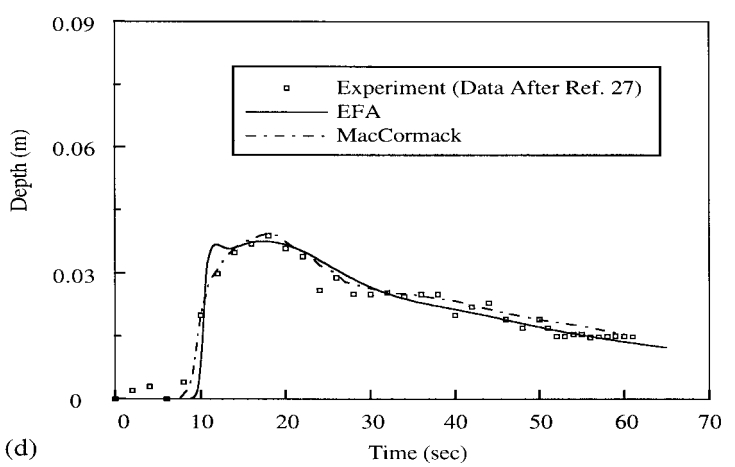

Figure 12 (*Continued*)

9. CONCLUSIONS

A depth-averaged explicit–finite–analytic (EFA) numerical model has been developed and applied to two-dimensional free-surface flow problems. The governing equations are derived in the general curvilinear co-ordinate system by full transformation. In addition, a body-fitted grid system is generated in the proposed model for the purpose of properly specifying irregular boundaries of the open channels. The non-linear convective terms of the momentum equations

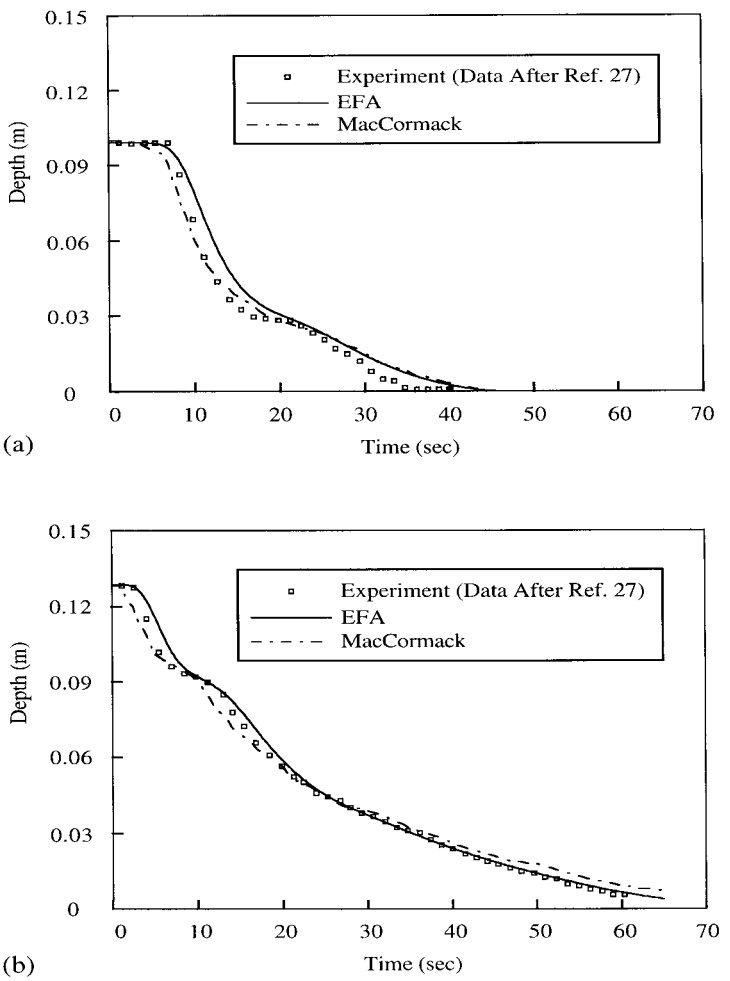

Figure 13. Comparison between computational and experimental depth hydrographs for slope = 0.006; (a) $X = 0$ m, (b) $X = 4.5$ m, (c) $X = 11$ m, (d) $X = 18.5$ m.

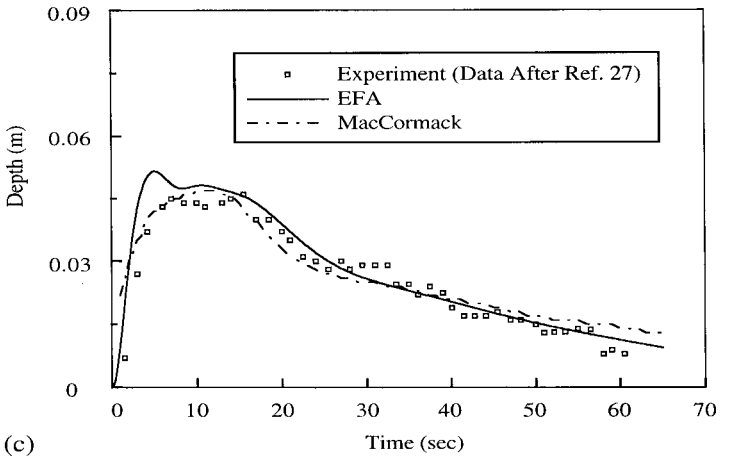

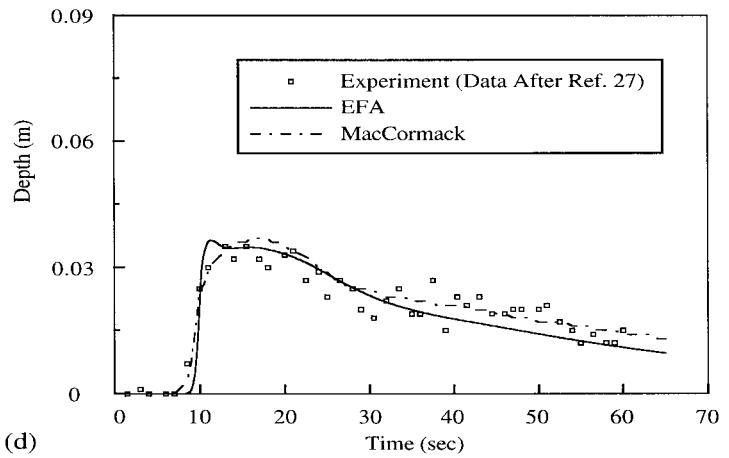

Figure 13 (*Continued*)

are discretized based on the EFA method. The EFA method has the advantage of simplicity and is numerically formulated from concept of mathematical exact solution of equation. Three examples with different degrees of numerical difficulties are illustrated in this paper to verify the capability of the proposed model. They are the convection-dominated flow with strong curvature of streamline, hydraulic jumps with the presence of sub-critical and supercritical flow regimes simultaneously in different regions or in sequence in time, and unsteady dam-break flows in the non-prismatic channel with alternatively wet and dry bed. Comparisons between numerical results and experimental data show a reasonably good agreement.

ACKNOWLEDGMENTS

This research was supported by the National Science Council of the Republic of China, under Grant No. NSC-85-2211-E-009-33. The authors are grateful to W.F. Tsai and C.Y. Shen for their valuable advice during the course of this study.

APPENDIX A. NON-ORTHOGONAL DEPTH-AVERAGED GOVERNING EQUATIONS

A.1. Continuity equation

$$\frac{\partial h}{\partial t}+g_{11}^{-0.5}g_{22}^{-0.5}\frac{\partial[g_{22}^{0.5}\cdot\bar{u}h]}{\partial\xi}+g_{11}^{-0.5}g_{22}^{-0.5}\frac{\partial[g_{11}^{0.5}\cdot\bar{v}h]}{\partial\eta}$$
$$+\frac{1}{2}g_{11}^{-0.5}\left(g^{11}\frac{\partial g_{11}}{\partial\xi}+2g^{12}\frac{\partial g_{12}}{\partial\xi}+g^{22}\frac{\partial g_{22}}{\partial\xi}-g_{22}^{-1}\frac{\partial g_{22}}{\partial\xi}-g_{11}^{-1}\frac{\partial g_{11}}{\partial\xi}\right)\cdot\bar{u}h$$
$$+\frac{1}{2}g_{22}^{-0.5}\left(g^{11}\frac{\partial g_{11}}{\partial\eta}+2g^{12}\frac{\partial g_{12}}{\partial\eta}+g^{22}\frac{\partial g_{22}}{\partial\eta}-g_{11}^{-1}\frac{\partial g_{11}}{\partial\eta}-g_{22}^{-1}\frac{\partial g_{22}}{\partial\eta}\right)\cdot\bar{v}h=0$$

A.2. ξ-Direction momentum equation

$$\frac{\partial\bar{u}}{\partial t}+g_{11}^{-0.5}\cdot\bar{u}\frac{\partial\bar{u}}{\partial\xi}+g_{22}^{-0.5}\cdot\bar{v}\frac{\partial\bar{u}}{\partial\eta}$$
$$+\frac{1}{2}g_{11}^{-0.5}\left(g^{11}\frac{\partial g_{11}}{\partial\xi}+2g^{12}\frac{\partial g_{12}}{\partial\xi}-g^{12}\frac{\partial g_{11}}{\partial\eta}-g_{11}^{-1}\frac{\partial g_{11}}{\partial\xi}\right)\cdot[\bar{u}^2]$$
$$+\frac{1}{2}g_{22}^{-0.5}\left(g^{11}\frac{\partial g_{11}}{\partial\eta}+g^{12}\frac{\partial g_{22}}{\partial\xi}-g_{11}^{-1}\frac{\partial g_{11}}{\partial\eta}\right)\cdot[\bar{u}\bar{v}]$$
$$+\frac{1}{2}g_{22}^{-0.5}\left(g^{11}\frac{\partial g_{11}}{\partial\eta}+g^{12}\frac{\partial g_{22}}{\partial\xi}\right)\cdot[\bar{u}\bar{v}]$$
$$+\frac{1}{2}g_{11}^{0.5}g_{22}^{-1}\left(2g^{11}\frac{\partial g_{12}}{\partial\eta}-g^{11}\frac{\partial g_{22}}{\partial\xi}+g^{12}\frac{\partial g_{22}}{\partial\eta}\right)\cdot[\bar{v}^2]$$
$$+\frac{1}{h}g_{11}^{-0.5}g_{22}^{-0.5}\frac{\partial}{\partial\xi}\left[g_{22}^{0.5}\frac{1}{N(N+2)}\bar{u}^2h\right]+\frac{1}{h}g_{11}^{-0.5}g_{22}^{-0.5}\frac{\partial}{\partial\eta}\left[g_{11}^{0.5}\frac{1}{N(N+2)}\bar{u}\bar{v}h\right]$$
$$+\frac{1}{2}g_{11}^{-0.5}\left(g^{11}\frac{\partial g_{11}}{\partial\xi}+2g^{12}\frac{\partial g_{12}}{\partial\xi}-g^{12}\frac{\partial g_{11}}{\partial\eta}-g_{11}^{-1}\frac{\partial g_{11}}{\partial\xi}\right)\cdot\left[\frac{1}{N(N+2)}\bar{u}^2\right]$$
$$+\frac{1}{2}g_{22}^{-0.5}\left(g^{11}\frac{\partial g_{11}}{\partial\eta}+g^{12}\frac{\partial g_{22}}{\partial\xi}-g_{11}^{-1}\frac{\partial g_{11}}{\partial\eta}\right)\cdot\left[\frac{1}{N(N+2)}\bar{u}\bar{v}\right]$$

$$+\frac{1}{2}g_{22}^{-0.5}\left(g^{11}\frac{\partial g_{11}}{\partial\eta}+g^{12}\frac{\partial g_{22}}{\partial\xi}\right)\cdot\left[\frac{1}{N(N+2)}\bar{u}\bar{v}\right]$$

$$+\frac{1}{2}g_{11}^{0.5}g_{22}^{-1}\left(2g^{11}\frac{\partial g_{12}}{\partial\eta}-g^{11}\frac{\partial g_{22}}{\partial\xi}+g^{12}\frac{\partial g_{22}}{\partial\eta}\right)\cdot\left[\frac{1}{N(N+2)}\bar{v}^2\right]$$

$$+\frac{1}{2}g_{11}^{-0.5}\left(g^{11}\frac{\partial g_{11}}{\partial\xi}+2g^{12}\frac{\partial g_{12}}{\partial\xi}+g^{22}\frac{\partial g_{22}}{\partial\xi}-g_{22}^{-1}\frac{\partial g_{22}}{\partial\xi}-g_{11}^{-1}\frac{\partial g_{11}}{\partial\xi}\right)\cdot\left[\frac{1}{N(N+2)}\bar{u}^2\right]$$

$$+\frac{1}{2}g_{22}^{-0.5}\left(g^{11}\frac{\partial g_{11}}{\partial\eta}+2g^{12}\frac{\partial g_{12}}{\partial\xi}-g_{11}^{-1}\frac{\partial g_{11}}{\partial\eta}+g^{22}\frac{\partial g_{22}}{\partial\eta}-g_{22}^{-1}\frac{\partial g_{22}}{\partial\eta}\right)\cdot\left[\frac{1}{N(N+2)}\bar{u}\bar{v}\right]$$

$$+\frac{1}{h}g_{11}^{-0.5}\frac{\partial}{\partial\xi}\left[\int_{z_b}^{z_s}\tilde{}\,\tilde{u^{\gamma 2}}\tilde{}\;\mathrm{d}z\right]+\frac{1}{h}g_{22}^{-0.5}\frac{\partial}{\partial\eta}\left[\int_{z_b}^{z_s}\tilde{}\,\tilde{u'}\tilde{v'}\tilde{}\;\mathrm{d}z\right]$$

$$+\frac{1}{2h}g_{11}^{-0.5}\left[2g^{11}\frac{\partial g_{11}}{\partial\xi}+4g^{12}\frac{\partial g_{12}}{\partial\xi}-g^{12}\frac{\partial g_{11}}{\partial\eta}+g^{22}\frac{\partial g_{22}}{\partial\xi}-2g_{11}^{-1}\frac{\partial g_{11}}{\partial\xi}\right]\int_{z_b}^{z_s}\tilde{}\,\tilde{u^{\gamma 2}}\tilde{}\;\mathrm{d}z$$

$$+\frac{1}{2h}g_{22}^{-0.5}\left[3g^{11}\frac{\partial g_{11}}{\partial\eta}+2g^{12}\frac{\partial g_{22}}{\partial\xi}-g_{11}^{-1}\frac{\partial g_{11}}{\partial\eta}-g_{22}^{-1}\frac{\partial g_{22}}{\partial\eta}+2g^{12}\frac{\partial g_{12}}{\partial\eta}+g^{22}\frac{\partial g_{22}}{\partial\eta}\right]$$
$$\times\int_{z_b}^{z_s}\tilde{}\,\tilde{u'}\tilde{v'}\tilde{}\;\mathrm{d}z$$

$$+\frac{1}{2h}g_{11}^{0.5}g_{22}^{-1}\left[2g^{11}\frac{\partial g_{12}}{\partial\eta}-g^{11}\frac{\partial g_{22}}{\partial\xi}+g^{12}\frac{\partial g_{22}}{\partial\eta}\right]\int_{z_b}^{z_s}\tilde{}\,\tilde{v^{\gamma 2}}\tilde{}\;\mathrm{d}z$$

$$=-g\cdot g_{11}^{0.5}g^{11}\frac{\partial(z_b+h)}{\partial\xi}-g\cdot g_{11}^{0.5}g^{12}\frac{\partial(z_b+h)}{\partial\eta}$$

$$+\frac{v}{h}\cdot\left\{g^{11}\frac{\partial}{\partial\xi}\left[\int_{z_b}^{z_s}\frac{\partial u}{\partial\xi}\,\mathrm{d}z\right]-g^{11}\left[\frac{\partial u_s}{\partial\xi}\frac{\partial z_s}{\partial\xi}\right]+2g^{12}\frac{\partial}{\partial\xi}\left[\int_{z_b}^{z_s}\frac{\partial u}{\partial\eta}\,\mathrm{d}z\right]\right.$$

$$\left.-2g^{12}\left[\frac{\partial u_s}{\partial\eta}\frac{\partial z_s}{\partial\xi}\right]+g^{22}\frac{\partial}{\partial\eta}\left[\int_{z_b}^{z_s}\frac{\partial u}{\partial\eta}\,\mathrm{d}z\right]-g^{22}\left[\frac{\partial u_s}{\partial\eta}\frac{\partial z_s}{\partial\eta}\right]+\frac{\partial u_s}{\partial z}-\frac{\partial u_b}{\partial z}\right.$$

$$+\left[\frac{1}{2}(g^{11})^2\frac{\partial g_{11}}{\partial\xi}+g^{11}g^{12}\frac{\partial g_{12}}{\partial\xi}-\frac{1}{2}g^{11}g^{12}\frac{\partial g_{11}}{\partial\eta}-g^{11}g^{22}\frac{\partial g_{12}}{\partial\eta}\right.$$

$$\left.\left.+\frac{1}{2}g^{11}g^{22}\frac{\partial g_{22}}{\partial\xi}-\frac{1}{2}g^{12}g^{22}\frac{\partial g_{22}}{\partial\eta}-g_{11}^{-1}g^{11}\frac{\partial g_{11}}{\partial\xi}-g_{11}^{-1}g^{12}\frac{\partial g_{11}}{\partial\eta}\right]\cdot\left[\int_{z_b}^{z_s}\frac{\partial u}{\partial\xi}\,\mathrm{d}z\right]\right.$$

$$+\left[\frac{1}{2}g^{11}g^{12}\frac{\partial g_{11}}{\partial\xi}-g^{11}g^{22}\frac{\partial g_{12}}{\partial\xi}+\frac{3}{2}g^{11}g^{22}\frac{\partial g_{11}}{\partial\eta}-2(g^{12})^2\frac{\partial g_{11}}{g\eta}-g^{12}g^{22}\frac{\partial g_{12}}{\partial\eta}+\frac{1}{2}g^{12}g^{22}\frac{\partial g_{22}}{\partial\xi}\right.$$

$$
\begin{aligned}
&-\frac{1}{2}(g^{22})^2\frac{\partial g_{22}}{\partial \eta}-g_{11}^{-1}g^{12}\frac{\partial g_{11}}{\partial \xi}-g_{11}^{-1}g^{22}\frac{\partial g_{11}}{\partial \eta}+2(g^{12})^2\frac{\partial g_{12}}{\partial \xi}\Bigg]\cdot\left[\int_{z_b}^{z_s}\frac{\partial u}{\partial \eta}\,\mathrm{d}z\right]\\
&+g_{11}^{0.5}g_{22}^{-0.5}\left[(g^{11})^2\frac{\partial g_{11}}{\partial \eta}+2g^{11}g^{12}\frac{\partial g_{12}}{\partial \eta}+(g^{12})^2\frac{\partial g_{12}}{\partial \eta}\right]\cdot\left[\int_{z_b}^{z_s}\frac{\partial v}{\partial \xi}\,\mathrm{d}z\right]\\
&+g_{11}^{0.5}g_{22}^{-0.5}\left[g^{11}g^{12}\frac{\partial g_{11}}{\partial \eta}+(g^{12})^2\frac{\partial g_{22}}{\partial \xi}+2g^{11}g^{22}\frac{\partial g_{12}}{\partial \eta}-g^{11}g^{22}\frac{\partial g_{22}}{\partial \xi}+g^{12}g^{22}\frac{\partial g_{22}}{\partial \eta}\right]\\
&\quad\cdot\left[\int_{z_b}^{z_s}\frac{\partial v}{\partial \eta}\,\mathrm{d}z\right]\\
&-\frac{1}{2}\left[g_{11}^{-1}\frac{\partial g_{11}}{\partial \xi^n}\frac{\partial g^{mn}}{\partial \xi^m}+g^{mn}g_{11}^{-1}\frac{\partial^2 g_{11}}{\partial \xi^m\partial \xi^n}-\frac{3}{2}g^{mn}g_{11}^{-2}\frac{\partial g_{11}}{\partial \xi^n}\frac{\partial g_{11}}{\partial \xi^m}+\Gamma^n_{nm}g^{mk}g_{11}^{-1}\frac{\partial g_{11}}{\partial \xi^k}\right]\cdot\bar{u}h\\
&+\Bigg[-g^{mn}g_{11}^{0.5}g_{ss}^{-1.5}\Gamma^1_{ns}\frac{\partial g_{ss}}{\partial \xi^m}+\frac{1}{2}g^{mn}g_{11}^{0.5}g_{ss}^{-0.5}\left(\frac{\partial g_{ks}}{\partial \xi^n}+\frac{\partial g_{kn}}{\partial \xi^s}-\frac{\partial g_{ns}}{\partial \xi^k}\right)\frac{\partial g^{1k}}{\partial \xi^m}\\
&+\frac{1}{2}g^{mn}g_{11}^{0.5}g_{ss}^{-0.5}g^{1k}\left(\frac{\partial^2 g_{ks}}{\partial \xi^n\partial \xi^m}+\frac{\partial^2 g_{kn}}{\partial \xi^m\partial \xi^s}-\frac{\partial^2 g_{ns}}{\partial \xi^m\partial \xi^k}\right)\\
&+g_{11}^{0.5}g_{ss}^{-0.5}\Gamma^1_{ns}\frac{\partial g^{mn}}{\partial \xi^m}+g^{mk}g_{11}^{0.5}g_{ss}^{-0.5}\Gamma^n_{mn}\Gamma^1_{ks}+g^{mk}g_{11}^{0.5}g_{ss}^{-0.5}\Gamma^1_{kn}\Gamma^n_{ms}\Bigg]\cdot\bar{V}(s)h\Bigg\}
\end{aligned}
$$

A.3. η-Direction momentum equation

$$
\begin{aligned}
&\frac{\partial \bar{v}}{\partial t}+g_{11}^{-0.5}\cdot\bar{u}\frac{\partial \bar{v}}{\partial \xi}+g_{22}^{-0.5}\cdot\bar{v}\frac{\partial \bar{v}}{\partial \eta}\\
&+\frac{1}{2}g_{22}^{0.5}g_{11}^{-1}\left(2g^{22}\frac{\partial g_{12}}{\partial \xi}-g^{22}\frac{\partial g_{11}}{\partial \eta}+g^{12}\frac{\partial g_{11}}{\partial \xi}\right)\cdot[\bar{u}^2]\\
&+\frac{1}{2}g_{11}^{-0.5}\left(g^{22}\frac{\partial g_{22}}{\partial \xi}+g^{12}\frac{\partial g_{11}}{\partial \eta}\right)\cdot[\bar{u}\bar{v}]\\
&+\frac{1}{2}g_{11}^{-0.5}\left(g^{22}\frac{\partial g_{22}}{\partial \xi}+g^{12}\frac{\partial g_{11}}{\partial \eta}-g_{22}^{-1}\frac{\partial g_{22}}{\partial \xi}\right)\cdot[\bar{u}\bar{v}]\\
&+\frac{1}{2}g_{22}^{-0.5}\left(g^{22}\frac{\partial g_{22}}{\partial \eta}+2g^{12}\frac{\partial g_{12}}{\partial \eta}-g^{12}\frac{\partial g_{22}}{\partial \xi}-g_{22}^{-1}\frac{\partial g_{22}}{\partial \eta}\right)\cdot[\bar{v}^2]\\
&+\frac{1}{h}g_{11}^{-0.5}g_{22}^{-0.5}\frac{\partial}{\partial \xi}\left[g_{22}^{0.5}\frac{1}{N(N+2)}\bar{u}\bar{v}h\right]+\frac{1}{h}g_{11}^{-0.5}g_{22}^{-0.5}\frac{\partial}{\partial \eta}\left[g_{11}^{0.5}\frac{1}{N(N+2)}\bar{v}^2h\right]\\
&+\frac{1}{2}g_{22}^{0.5}g_{11}^{-1}\left(2g^{22}\frac{\partial g_{12}}{\partial \xi}-g^{22}\frac{\partial g_{11}}{\partial \eta}+g^{12}\frac{\partial g_{11}}{\partial \xi}\right)\cdot\left[\frac{1}{N(N+2)}\bar{u}^2\right]
\end{aligned}
$$

$$+\frac{1}{2}g_{11}^{-0.5}\left(g^{22}\frac{\partial g_{22}}{\partial \xi}+g^{12}\frac{\partial g_{11}}{\partial \eta}\right)\cdot\left[\frac{1}{N(N+2)}\bar{u}\bar{v}\right]$$

$$+\frac{1}{2}g_{11}^{-0.5}\left(g^{22}\frac{\partial g_{22}}{\partial \xi}+g^{12}\frac{\partial g_{11}}{\partial \eta}-g_{22}^{-1}\frac{\partial g_{22}}{\partial \xi}\right)\cdot\left[\frac{1}{N(N+2)}\bar{u}\bar{v}\right]$$

$$+\frac{1}{2}g_{22}^{-0.5}\left(g^{22}\frac{\partial g_{22}}{\partial \eta}+2g^{12}\frac{\partial g_{12}}{\partial \eta}-g^{12}\frac{\partial g_{22}}{\partial \xi}-g_{22}^{-1}\frac{\partial g_{22}}{\partial \eta}\right)\cdot\left[\frac{1}{N(N+2)}\bar{v}^2\right]$$

$$+\frac{1}{2}g_{11}^{-0.5}\left(g^{22}\frac{\partial g_{22}}{\partial \xi}+2g^{12}\frac{\partial g_{12}}{\partial \xi}+g^{11}\frac{\partial g_{11}}{\partial \xi}-g_{22}^{-1}\frac{\partial g_{22}}{\partial \xi}-g_{11}^{-1}\frac{\partial g_{11}}{\partial \xi}\right)\cdot\left[\frac{1}{N(N+2)}\bar{u}\bar{v}\right]$$

$$+\frac{1}{2}g_{22}^{-0.5}\left(g^{22}\frac{\partial g_{22}}{\partial \eta}+2g^{12}\frac{\partial g_{12}}{\partial \eta}+g^{11}\frac{\partial g_{11}}{\partial \eta}-g_{11}^{-1}\frac{\partial g_{11}}{\partial \eta}-g_{22}^{-1}\frac{\partial g_{22}}{\partial \eta}\right)\cdot\left[\frac{1}{N(N+2)}\bar{v}^2\right]$$

$$+\frac{1}{h}g_{22}^{-0.5}\frac{\partial}{\partial \eta}\left[\int_{z_b}^{z_s}\tilde{\sim}\,\tilde{v}'\tilde{\mathcal{Z}}\,\tilde{\sim}\,\mathrm{d}z\right]+\frac{1}{h}g_{11}^{-0.5}\frac{\partial}{\partial \xi}\left[\int_{z_b}^{z_s}\tilde{\sim}\,\tilde{u}'\tilde{v}'\tilde{\sim}\,\tilde{\sim}\,\mathrm{d}z\right]$$

$$+\frac{1}{2h}g_{22}^{-0.5}\left[2g^{22}\frac{\partial g_{22}}{\partial \eta}+4g^{12}\frac{\partial g_{12}}{\partial \eta}-g^{12}\frac{\partial g_{22}}{\partial \xi}+g^{11}\frac{\partial g_{11}}{\partial \eta}-2g_{22}^{-1}\frac{\partial g_{22}}{\partial \eta}\right]\int_{z_b}^{z_s}\tilde{\sim}\,\tilde{v}'\tilde{\mathcal{Z}}\,\tilde{\sim}\,\mathrm{d}z$$

$$+\frac{1}{2h}g_{11}^{-0.5}\left[3g^{22}\frac{\partial g_{22}}{\partial \xi}+2g^{12}\frac{\partial g_{11}}{\partial \eta}-g_{22}^{-1}\frac{\partial g_{22}}{\partial \xi}-g_{11}^{-1}\frac{\partial g_{11}}{\partial \xi}+2g^{12}\frac{\partial g_{12}}{\partial \xi}+g^{11}\frac{\partial g_{11}}{\partial \xi}\right]\int_{z_b}^{z_s}\tilde{\sim}\,\tilde{u}'\tilde{v}'\tilde{\sim}\,\mathrm{d}z$$

$$+\frac{1}{2h}g_{22}^{0.5}g_{11}^{-1}\left[2g^{22}\frac{\partial g_{12}}{\partial \xi}-g^{22}\frac{\partial g_{11}}{\partial \eta}+g^{12}\frac{\partial g_{11}}{\partial \xi}\right]\int_{z_b}^{z_s}\tilde{\sim}\,\tilde{u}'\tilde{\mathcal{Z}}\,\tilde{\sim}\,\mathrm{d}z$$

$$=-g\cdot g_{22}^{0.5}g^{22}\frac{\partial(z_b+h)}{\partial \eta}-g\cdot g_{22}^{0.5}g^{12}\frac{\partial(z_b+h)}{\partial \xi}$$

$$+\frac{v}{h}\cdot\left\{g^{22}\frac{\partial}{\partial \eta}\left[\int_{z_b}^{z_s}\frac{\partial v}{\partial \eta}\,\mathrm{d}z\right]-g^{22}\left[\frac{\partial v_s}{\partial \eta}\frac{\partial z_s}{\partial \eta}\right]+2g^{12}\frac{\partial}{\partial \eta}\left[\int_{z_b}^{z_s}\frac{\partial v}{\partial \xi}\,\mathrm{d}z\right]\right.$$

$$\left.-2g^{12}\left[\frac{\partial v_s}{\partial \xi}\frac{\partial z_s}{\partial \eta}\right]+g^{11}\frac{\partial}{\partial \xi}\left[\int_{z_b}^{z_s}\frac{\partial v}{\partial \xi}\,\mathrm{d}z\right]-g^{11}\left[\frac{\partial v_s}{\partial \xi}\frac{\partial z_s}{\partial \xi}\right]+\frac{\partial v_s}{\partial z}-\frac{\partial v_b}{\partial z}\right.$$

$$+\left[\frac{1}{2}(g^{22})^2\frac{\partial g_{22}}{\partial \eta}+g^{22}g^{12}\frac{\partial g_{12}}{\partial \eta}-\frac{1}{2}g^{22}g^{12}\frac{\partial g_{22}}{\partial \xi}-g^{11}g^{22}\frac{\partial g_{12}}{\partial \xi}\right.$$

$$\left.\left.+\frac{1}{2}g^{11}g^{22}\frac{\partial g_{11}}{\partial \eta}-\frac{1}{2}g^{12}g^{11}\frac{\partial g_{11}}{\partial \xi}-g_{22}^{-1}g^{22}\frac{\partial g_{22}}{\partial \eta}-g_{22}^{-1}g^{12}\frac{\partial g_{22}}{\partial \xi}\right]\cdot\left[\int_{z_b}^{z_s}\frac{\partial v}{\partial \eta}\,\mathrm{d}z\right]\right.$$

$$+\left[\frac{1}{2}g^{22}g^{12}\frac{\partial g_{22}}{\partial \eta}-g^{11}g^{22}\frac{\partial g_{12}}{\partial \eta}+\frac{3}{2}g^{11}g^{22}\frac{\partial g_{22}}{\partial \xi}-2(g^{12})^2\frac{\partial g_{22}}{\partial \xi}-g^{12}g^{11}\frac{\partial g_{12}}{\partial \xi}\right.$$

$$+\frac{1}{2}g^{12}g^{11}\frac{\partial g_{11}}{\partial \eta}-\frac{1}{2}(g^{11})^2\frac{\partial g_{11}}{\partial \xi}-g_{22}^{-1}g^{12}\frac{\partial g_{22}}{\partial \eta}-g_{22}^{-1}g^{11}\frac{\partial g_{22}}{\partial \xi}+2(g^{12})^2\frac{\partial g_{12}}{\partial \eta}\Bigg]\cdot\left[\int_{z_b}^{z_s}\frac{\partial v}{\partial \xi}\,\mathrm{d}z\right]$$

$$+g_{22}^{0.5}g_{11}^{-0.5}\left[(g^{22})^2\frac{\partial g_{22}}{\partial \xi}+2g^{22}g^{12}\frac{\partial g_{12}}{\partial \xi}+(g^{12})^2\frac{\partial g_{11}}{\partial \xi}\right]\cdot\left[\int_{z_b}^{z_s}\frac{\partial u}{\partial \eta}\,\mathrm{d}z\right]$$

$$+g_{22}^{0.5}g_{11}^{-0.5}\left[g^{22}g^{12}\frac{\partial g_{22}}{\partial \xi}+(g^{12})^2\frac{\partial g_{11}}{\partial \eta}+2g^{11}g^{22}\frac{\partial g_{12}}{\partial \xi}-g^{11}g^{22}\frac{\partial g_{11}}{\partial \eta}+g^{12}g^{11}\frac{\partial g_{11}}{\partial \xi}\right]\cdot\left[\int_{z_b}^{z_s}\frac{\partial u}{\partial \xi}\,\mathrm{d}z\right]$$

$$-\frac{1}{2}\left[g_{22}^{-1}\frac{\partial g_{22}}{\partial \xi^n}\frac{\partial g^{mn}}{\partial \xi^m}+g^{mn}g_{22}^{-1}\frac{\partial^2 g_{22}}{\partial \xi^m\partial \xi^n}-\frac{3}{2}g^{mn}g_{22}^{-2}\frac{\partial g_{22}}{\partial \xi^n}\frac{\partial g_{22}}{\partial \xi^m}+\Gamma_{nm}^{n}g^{mk}g_{22}^{-1}\frac{\partial g_{22}}{\partial \xi^k}\right]\cdot\bar{v}h$$

$$+\Bigg[-g^{mn}g_{22}^{0.5}g_{ss}^{-1.5}\Gamma_{ns}^{2}\frac{\partial g_{ss}}{\partial \xi^m}+\frac{1}{2}g^{mn}g_{22}^{0.5}g_{ss}^{-0.5}\left(\frac{\partial g_{ks}}{\partial \xi^n}+\frac{\partial g_{kn}}{\partial \xi^s}-\frac{\partial g_{ns}}{\partial \xi^k}\right)\frac{\partial g^{2k}}{\partial \xi^m}$$

$$+\frac{1}{2}g^{mn}g_{22}^{0.5}g_{ss}^{-0.5}g^{2k}\left(\frac{\partial^2 g_{ks}}{\partial \xi^n\partial \xi^m}+\frac{\partial^2 g_{kn}}{\partial \xi^m\partial \xi^s}-\frac{\partial^2 g_{ns}}{\partial \xi^m\partial \xi^k}\right)$$

$$+g_{22}^{0.5}g_{ss}^{-0.5}\Gamma_{ns}^{2}\frac{\partial g^{mn}}{\partial \xi^m}+g^{mk}g_{22}^{0.5}g_{ss}^{-0.5}\Gamma_{mn}^{n}\Gamma_{ks}^{2}+g^{mk}g_{22}^{0.5}g_{ss}^{-0.5}\Gamma_{kn}^{2}\Gamma_{ms}^{n}\Bigg]\cdot\bar{V}(s)h\Bigg\}$$

in which summation takes over m, n, k, and s, and the velocities u, v and elevation z with subscripts s and b represent the values at locations of water surface and channel bed respectively.

REFERENCES

1. Fennema RJ, Chaudhry MH. Explicit methods for 2D transient free-surface flows. *Journal of Hydraulic Engineering*, *ASCE* 1990; **116**(8): 1013–1034.
2. Benque JP, Cunge JA, Feuillet J, Hauguel A, Holly FM Jr. New method for tidal current computation. *Journal of Waterway*, *Port*, *Coastal and Ocean Division*, *ASCE* 1982; **108**(WW3): 396–417.
3. Chapman RS, Kuo CY. Application of the two-equation k–ε turbulence model to a two-dimensional, steady, free surface flow problem with separation. *International Journal for Numerical Methods in Fluids* 1985; **5**: 257–268.
4. Ye BJ, McCorquodale JA. Depth-averaged hydrodynamic model in curvilinear collocated grid. *Journal of Hydraulic Engineering*, *ASCE* 1997; **123**(5): 380–388.
5. Roe PL. Approximate Riemann solver, parameter vectors, and difference schemes. *Journal of Computers in Physics* 1981; **43**(2): 357–372.
6. Patankar SV. *Numerical Heat Transfer and Fluid Flow*. Hemisphere Publishing: Bristol, PA, 1980.
7. Dai W. Numerical solutions of unsteady Navier–Stokes equations using explicit finite analytic scheme. PhD thesis, Department of Applied Mathematics, University of Iowa, IA, 1994.
8. Katopodes N, Strelkoff T. Computing two-dimensional dam-break flood waves. *Journal of Hydraulic Division*, *ASCE* 1978; **104**(HY9): 1269–1288.
9. Gabutti B. On two upwind finite-difference schemes for hyperbolic equations in non-conservative form. *Computers and Fluids* 1983; **11**(3): 207–230.
10. Fennema RJ, Chaudhry MH. Implicit methods for two-dimensional unsteady free-surface flows. *Journal of Hydraulic Research* 1989; **27**(3): 321–332.

11. Molls T, Chaudhry MH, Khan KW. Numerical simulation of two-dimensional flow near a spur–dike. *Advances in Water Resources* 1995; **18**(4): 227–236.
12. Fraccarollo L, Toro EF. Experimental and numerical assessment of the shallow water model for two-dimensional dam-break type problems. *Journal of Hydraulic Research* 1995; **33**(6): 843–864.
13. Richmond MC, Chen HC, Patel VC. Equations of laminar and turbulent flows in general curvilinear coordinates. IIHR Report, No. 300, University of Iowa, IA, 1986.
14. Kuipers J, Vreugdenhil CB. Calculation of two-dimensional horizontal flow. Report S 163-1, Delft Hydraulic Laboratory, 1973.
15. Tingsanchali T, Maheswaran S. 2D depth-average flow computation near Groyne. *Journal of Hydraulic Engineering*, *ASCE* 1990; **116**(1): 71–86.
16. Bhallamudi SM, Chaudhry MH. Computation of flows in open-channel transitions. *Journal of Hydraulic Research* 1992; **30**(1): 77–95.
17. Boussinesq J. Essai sur la theorie des eaux courantes. In *Mem. Academy of Science XXIII*. Paris, 1877.
18. Falconer RA. Numerical modeling of tidal circulation in harbors. *Journal of Waterway*, *Port*, *Coastal and Ocean Division*, *ASCE* 1980; **106**(WW1): 31–48.
19. Durst F, Rastogi AK. Theoretical and experimental investigations of turbulent flows with separation. Proceedings of the International Symposium on Turbulent Shear Flows, I. Pennsylvania State University, University Park, PA, 1979; 208–219.
20. Shen CY. Numerical simulation of viscous flow using a solution-adaptive method. PhD dissertation, Department of Mechanical Engineering, Arizona State University, Tempe, AZ, 1991.
21. Garcia-Navarro P, Saviron JM. McCormack's method for the numerical simulation of one-dimensional discontinuous unsteady open channel flow. *Journal of Hydraulic Research* 1992; **30**(1): 95–105.
22. Ponce VM, Yabusaki SB. Modeling circulation in depth-averaged flow. *Journal of Hydraulic Division*, *ASCE* 1981; **107**(Hy11): 1501–1518.
23. Borthwick AGL, Akponasa GA. Reservoir flow prediction by contravariant shallow water equations. *Journal of Hydraulic Engineering*, *ASCE* 1997; **123**(5): 432–439.
24. Rahman M, Chaudhry MH. Simulation of hydraulic jump with grid adaptation. *Journal of Hydraulic Research* 1995; **33**(4): 555–568.
25. Gharangik AM, Chaudhry MH. Numerical simulation of hydraulic jump. *Journal of Hydraulic Engineering*, *ASCE* 1991; **117**(9): 1195–1211.
26. Elliot RC, Chaudhry MH. A wave propagation model for two-dimensional dam-break flows. *Journal of Hydraulic Research* 1992; **30**(4): 467–483.
27. Bellos CV, Soulis JV, Sakkas JG. Experimental investigation of two-dimensional dam-break induced flows. *Journal of Hydraulic Research* 1992; **30**(1): 47–63.

